

Deep Material Network: Overview, applications and current directions

Ting-Ju Wei¹, Wen-Ning Wan¹, Chuin-Shan Chen^{1,2*}

¹Department of Civil Engineering, National Taiwan University, No. 1, Sec. 4, Roosevelt Road, Taipei, 10617, Taiwan.

²Department of Materials Science and Engineering, National Taiwan University, No. 1, Sec. 4, Roosevelt Road, Taipei, 10617, Taiwan.

*Corresponding author(s). E-mail(s): dchen@ntu.edu.tw;
Contributing authors: d12521013@ntu.edu.tw; r12521603@ntu.edu.tw;

Abstract

Deep Material Network (DMN) has emerged as a powerful framework for multiscale material modeling, enabling efficient and accurate predictions of material behavior across different length scales. Unlike traditional machine learning approaches, the trainable parameters in DMN have direct physical interpretations, capturing the geometric characteristics of the microstructure rather than serving as purely statistical fitting parameters. Its hierarchical tree structure effectively encodes microstructural interactions and deformation mechanisms, allowing DMN to achieve a balance between accuracy and computational efficiency. This physics-informed architecture significantly reduces computational costs compared to direct numerical simulations while preserving essential microstructural physics. Furthermore, DMN can be trained solely on a linear elastic dataset while effectively extrapolating nonlinear responses during online prediction, making it a highly efficient and scalable approach for multiscale material modeling. This article provides a comprehensive review of DMN, detailing its motivation, underlying methodology, and recent advancements. We discuss key modeling aspects, including its hierarchical structure, training process, and the role of physics-based constraints in enhancing predictive accuracy. Furthermore, we highlight its applications in component-scale multiscale analysis and inverse parameter identification, demonstrating its capability to bridge microscale material behavior with macroscale engineering predictions. Finally, we discuss challenges and future directions in improving DMN's generalization capabilities and its potential extensions for broader applications in multiscale modeling.

Keywords: Deep material network, Multiscale modeling, Crystal plasticity, Hyperelasticity, Nonlinear plasticity

1 Introduction

Multiscale simulation methods are indispensable in computational mechanics for bridging the gap between microstructural features and macroscopic material behavior. Many engineering materials, such as polycrystals, composites, and porous media, exhibit pronounced heterogeneities that strongly influence their overall mechanical response. Accurately capturing these effects requires numerical approaches that incorporate microscale details while keeping the computational cost manageable.

A widely used strategy is the Representative Volume Element (RVE), which characterizes material heterogeneity statistically [1–5]. By applying macroscopic boundary conditions to the RVE, full-field methods like the finite element method (FEM) or fast Fourier transform (FFT)-based solvers can resolve the internal stress and strain distributions [6–10]. FEM offers flexibility with complex geometries, while FFT-based solvers leverage spectral methods for high efficiency in periodic domains.

Despite the accuracy of full-field simulations, their computational demands grow rapidly with microstructural complexity and nonlinear constitutive behavior. This cost becomes prohibitive for large-scale or real-time applications, prompting the development of surrogate models that approximate RVE responses at a fraction of the computational expense.

Machine-learning-based surrogates are a viable option for achieving significant speedups [11–18]. However, they typically rely on large training datasets and can struggle with extrapolation, necessitating retraining when microstructural morphology or constitutive behavior changes.

To overcome these issues, the Deep Material Network (DMN) was introduced as a physics-informed surrogate model for multiscale applications [19, 20]. DMN organizes the material response in a hierarchical, tree-based architecture, where each node corresponds to a local homogenization mechanism governed by analytical solutions. This approach directly encodes microstructural geometry into the network and requires training only on linear elastic stiffness data. Once trained, DMN excels at extrapolation to nonlinear regimes, capturing material nonlinearity to first-order accuracy [21].

This article provides a comprehensive overview of DMN, including its foundational principles, recent advancements, and applications. Section 2 introduces the original DMN architecture and its theoretical underpinnings. Section 3 discusses advanced enhancements and future directions, such as multiphysics coupling and broader generalization to diverse microstructures. Section 4 focuses on key applications, including component-scale multiscale analysis and inverse parameter identification. Finally, Section 5 summarizes the main findings and outlines future research directions for further extending DMN’s capabilities in multiscale modeling.

2 Deep Material Network

This section comprehensively reviews the original three-dimensional DMN architecture, detailing its hierarchical representation, theoretical foundation, and computational workflow. The discussion covers the network’s fundamental building blocks, the offline training process used to learn homogenization behavior, and the online prediction strategy for extrapolating nonlinear responses. An illustrative example demonstrates DMN’s capability to capture microstructural mechanical behavior with high efficiency and accuracy.

2.1 Hierarchical structure of DMN

DMN employs a hierarchical architecture to approximate the response of an RVE. As shown in Fig. 1, DMN is structured as a binary tree with N layers. The root node at Layer 1 represents the effective response of the RVE, while the bottom layer (N) contains 2^{N-1} nodes, each corresponding to a constituent material phase. Additionally, DMN consists of $2^N - 1$ fundamental building blocks, each denoted as \mathcal{B}_i^k , where i represents the depth of the network and k indexes the building block.

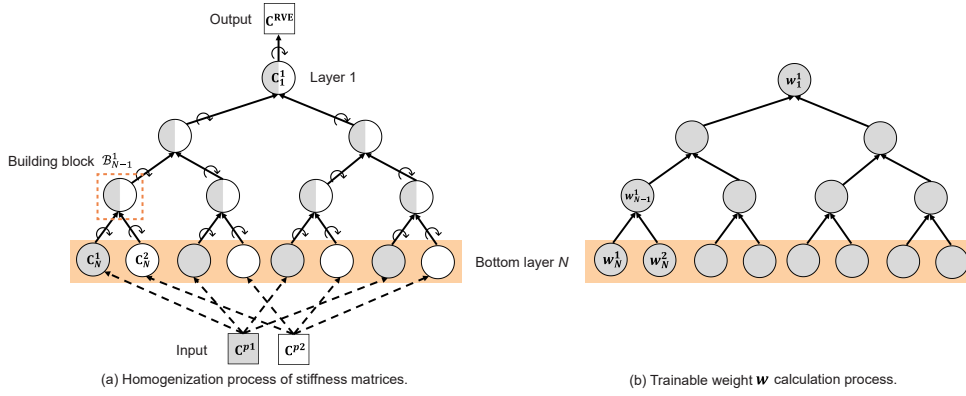


Fig. 1 Schematic representation of the data flow in the DMN framework. (a) Homogenization process of stiffness matrices, where the hierarchical network structure recursively aggregates local stiffness components to compute the effective stiffness \mathbf{C}^{RVE} . (b) Calculation of trainable weights \mathbf{w} , which parametrize the contributions of different building blocks within the hierarchical architecture.

To quantify the contribution of each constituent material phase, DMN introduces a weighting factor w_i^k at index k and layer i within each building block, as shown in Fig. 1(b). The trainable parameters z^k are defined at the bottom nodes, where the weighting factor w^k is activated using the ReLU function [22]:

$$w^k = \text{ReLU}(z^k), \quad k = 1, \dots, 2^N. \quad (1)$$

The weighting factor w^k represents the relative contribution of each bottom node. Due to the hierarchical nature of the DMN, the weighting factors are progressively

accumulated across layers and summed at the parent nodes, ensuring a consistent aggregation of contributions:

$$w_i^k = w_{i+1}^{2k} + w_{i+1}^{2k-1}. \quad (2)$$

This hierarchical accumulation enables DMN to capture the interaction between material phases while preserving physical consistency.

2.2 Mechanistic building block

This subsection provides the theoretical foundation for the DMN building block, which serves as the fundamental computational unit for homogenization. The homogenization function within each building block is derived based on the principles of linear elasticity. Consequently, the offline training data used in DMN is generated from linear elastic simulations. However, during online nonlinear extrapolation, DMN has been shown to serve as a first-order approximation of the nonlinear response [21].

Both stress σ and strain ε are expressed in terms of Cauchy stress and infinitesimal strain, adopting Mandel notation for consistency in the formulation:

$$\sigma = [\sigma_{11}, \sigma_{22}, \sigma_{33}, \sqrt{2}\sigma_{23}, \sqrt{2}\sigma_{13}, \sqrt{2}\sigma_{12}]^\top \equiv [\sigma_1, \sigma_2, \sigma_3, \sigma_4, \sigma_5, \sigma_6]^\top. \quad (3)$$

and

$$\varepsilon = [\varepsilon_{11}, \varepsilon_{22}, \varepsilon_{33}, \sqrt{2}\varepsilon_{23}, \sqrt{2}\varepsilon_{13}, \sqrt{2}\varepsilon_{12}]^\top \equiv [\varepsilon_1, \varepsilon_2, \varepsilon_3, \varepsilon_4, \varepsilon_5, \varepsilon_6]^\top. \quad (4)$$

The macroscopic stress-strain relationship is given by:

$$\bar{\sigma} = \bar{\mathbf{C}} : \bar{\varepsilon}. \quad (5)$$

For a building block consisting of two phases, denoted as phase 1 and phase 2, the local stress-strain relationships are:

$$\sigma^\alpha = \bar{\mathbf{C}}^\alpha : \varepsilon^\alpha, \quad \alpha = 1, 2. \quad (6)$$

where $\bar{\mathbf{C}}^1$ and $\bar{\mathbf{C}}^2$ represent the homogenized stiffness matrices of phases 1 and 2, respectively.

For a building block at index k and layer i , the contribution of each phase can be quantified using the volume fractions f^1 and f^2 , which are computed as:

$$f^\alpha = \frac{w_{i+1}^{2k+\alpha-2}}{w_{i+1}^{2k} + w_{i+1}^{2k-1}}, \quad \alpha = 1, 2. \quad (7)$$

These volume fractions characterize the relative contributions of phases 1 and 2 within the building block.

Each building block at depth i and index k performs two sequential operations, as illustrated in Fig. 2:

1. *Stiffness homogenization*: Computes an intermediate homogenized stiffness matrix \mathbf{C}_i^k by aggregating the stiffness properties of its child nodes.

2. *Rotation*: Transforms the intermediate homogenized stiffness \mathbf{C}_i^k into $\bar{\mathbf{C}}_i^k$, enabling a more flexible representation of the homogenization function. The rotation operation is parameterized by the trainable angles α_i^k , β_i^k , and γ_i^k , which define the local coordinate transformation for each building block.

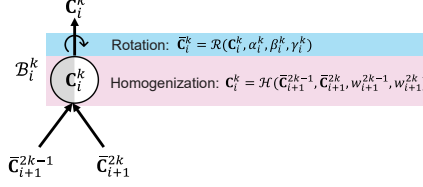


Fig. 2 Schematic illustration of the homogenization process within a building block \mathcal{B}_i^k .

2.2.1 Stiffness homogenization function

The stiffness homogenization function \mathcal{H} in DMN is derived based on the interfacial equilibrium condition, yielding an analytical form for the two-phase stiffness matrix homogenization. The interface between the two phases is assumed to be normal to the 3-direction, where strain compatibility is enforced in the 1-2 directions, while force equilibrium is satisfied in the 3-direction. A detailed derivation can be found in [20]. Following this derivation, the intermediate homogenized stiffness matrix \mathbf{C} is computed as:

$$\begin{aligned} \mathbf{C} &= \mathcal{H}(\bar{\mathbf{C}}^1, \bar{\mathbf{C}}^2, w^1, w^2) \\ &= f_1 \bar{\mathbf{C}}^1 \varepsilon^1 + f_2 \bar{\mathbf{C}}^2 \varepsilon^2 \\ &= \bar{\mathbf{C}}^2 - f^1 \Delta \mathbf{C} \mathbf{s}^1. \end{aligned} \quad (8)$$

where $\Delta \mathbf{C} = \bar{\mathbf{C}}^1 - \bar{\mathbf{C}}^2$ is the stiffness difference between the two phases, and \mathbf{s}^1 is the strain concentration tensor of phase 1, which determines the strain of phase 1 within the building block.

The strain concentration tensor \mathbf{s}^1 satisfies:

$$\varepsilon^1 = \mathbf{s}^1 \varepsilon, \quad \mathbf{s}_{11}^1 = \mathbf{s}_{22}^1 = \mathbf{s}_{66}^1 = 1, \quad \mathbf{s}_{([3,4,5],:)}^1 = \mathbf{s}_{3 \times 6}. \quad (9)$$

where the subscripts denote the row and column indices of the respective submatrix.

The submatrix $\mathbf{s}_{3 \times 6}$ is given by:

$$\mathbf{s}_{3 \times 6} = (\hat{\mathbf{C}}_{345})^{-1} \begin{bmatrix} f^2 \Delta C_{11} & f^2 \Delta C_{23} & \bar{C}_{33}^2 & \bar{C}_{34}^2 & \bar{C}_{35}^2 & f^2 \Delta C_{36} \\ f^2 \Delta C_{14} & f^2 \Delta C_{24} & \bar{C}_{34}^2 & \bar{C}_{44}^2 & \bar{C}_{45}^2 & f^2 \Delta C_{46} \\ f^2 \Delta C_{15} & f^2 \Delta C_{25} & \bar{C}_{35}^2 & \bar{C}_{45}^2 & \bar{C}_{55}^2 & f^2 \Delta C_{56} \end{bmatrix}. \quad (10)$$

where

$$\hat{\mathbf{C}} = f^2 \bar{\mathbf{C}}^1 + f^1 \bar{\mathbf{C}}^2 \quad (11)$$

and

$$\hat{\mathbf{C}}_{345} = \begin{bmatrix} \hat{C}_{33} & \hat{C}_{34} & \hat{C}_{35} \\ \hat{C}_{34} & \hat{C}_{44} & \hat{C}_{45} \\ \hat{C}_{35} & \hat{C}_{45} & \hat{C}_{55} \end{bmatrix}. \quad (12)$$

Here, the subscripts in ΔC and \hat{C} denote the corresponding row and column indices of the matrices $\Delta \mathbf{C}$ and $\hat{\mathbf{C}}$, respectively.

2.2.2 Rotation function

The rotation function \mathcal{R} in DMN is parameterized using the Tait-Bryan angles (α, β, γ) . The corresponding rotation matrix \mathbf{R} is expressed as the product of three elemental rotation matrices:

$$\mathbf{R}(\alpha, \beta, \gamma) = \mathbf{X}(\alpha)\mathbf{Y}(\beta)\mathbf{Z}(\gamma). \quad (13)$$

This rotation matrix is used to transform the intermediate homogenized stiffness matrix \mathbf{C} , obtained from Eq (8), into its rotated counterpart $\bar{\mathbf{C}}$:

$$\bar{\mathbf{C}} = \mathbf{R}^{-1}(\alpha, \beta, \gamma)\mathbf{C}\mathbf{R}(\alpha, \beta, \gamma) \quad (14)$$

The individual elemental rotation matrices $\mathbf{X}(\alpha)$, $\mathbf{Y}(\beta)$, and $\mathbf{Z}(\gamma)$ define rotations about the x -, y -, and z -axes, respectively. The subscripts in the following equations indicate the positions of the corresponding matrix components in the elemental rotation matrices, structured in Mandel notation:

$$\begin{aligned} \mathbf{X}_{(1,1)} &= 1, \mathbf{X}_{([2,3,4],[2,3,4])}(\alpha) = \mathbf{r}^p(\alpha), \mathbf{X}_{([5,6],[5,6])}(\alpha) = \mathbf{r}^\nu(\alpha); \\ \mathbf{Y}_{(2,2)} &= 1, \mathbf{Y}_{([1,3,5],[1,3,5])}(\beta) = \mathbf{r}^p(-\beta), \mathbf{Y}_{([4,6],[4,6])}(\beta) = \mathbf{r}^\nu(-\beta); \\ \mathbf{Z}_{(3,3)} &= 1, \mathbf{Z}_{([1,2,6],[1,2,6])}(\gamma) = \mathbf{r}^p(\gamma), \mathbf{Z}_{([4,5],[4,5])}(\gamma) = \mathbf{r}^\nu(\gamma); \end{aligned} \quad (15)$$

Here, \mathbf{r}^p and \mathbf{r}^ν denote the in-plane and out-of-plane rotation matrices, respectively. Given an arbitrary input angle θ , these matrices are defined as:

$$\begin{aligned} \mathbf{r}^p(\theta) &= \begin{bmatrix} \cos^2 \theta & \sin^2 \theta & \sqrt{2} \sin \theta \cos \theta \\ \sin^2 \theta & \cos^2 \theta & -\sqrt{2} \sin \theta \cos \theta \\ -\sqrt{2} \sin \theta \cos \theta & \sqrt{2} \sin \theta \cos \theta & \cos^2 \theta - \sin^2 \theta \end{bmatrix} \\ \mathbf{r}^\nu(\theta) &= \begin{bmatrix} \cos \theta & -\sin \theta \\ \sin \theta & \cos \theta \end{bmatrix} \end{aligned} \quad (16)$$

2.3 Offline training

The offline training process in DMN represents the overall homogenization procedure. It takes as input the stiffness matrices of two constituent phases, denoted as \mathbf{C}^{p1} and \mathbf{C}^{p2} , and outputs the homogenized stiffness matrix, \mathbf{C}^{DMN} , as formulated in Eq. (17). The trainable parameters of DMN are denoted collectively as $(\hat{z}, \hat{\alpha}, \hat{\beta}, \hat{\gamma})$ for brevity.

$$\mathbf{C}^{\text{DMN}} = \mathcal{DMN}(\mathbf{C}^{p1}, \mathbf{C}^{p2}, z^{k=1, \dots, 2^{N-1}}, \alpha_{i=1, \dots, N}^{k=1, \dots, 2^{i-1}}, \beta_{i=1, \dots, N}^{k=1, \dots, 2^{i-1}}, \gamma_{i=1, \dots, N}^{k=1, \dots, 2^{i-1}}) \quad (17)$$

The DMN dataset consists of stiffness matrices, where each data point is a triplet $(\mathbf{C}^{p1}, \mathbf{C}^{p2}, \mathbf{C}^{\text{DNS}})$. Here, \mathbf{C}^{p1} and \mathbf{C}^{p2} represent the stiffness matrices of the individual phases, while \mathbf{C}^{DNS} corresponds to the homogenized stiffness matrix obtained from DNS. The goal is to leverage the phase contrast between \mathbf{C}^{p1} and \mathbf{C}^{p2} , enabling DMN to learn the underlying geometric characteristics of the RVE.

The loss function \mathcal{L} is defined as follows, incorporating a regularization term:

$$\mathcal{L} = \frac{1}{2N_s} \sum_s \mathcal{L}_{stiff} + \lambda \left(\sum_j (\text{ReLU}(z^j) - 2^{N-2})^2 \right) \quad (18)$$

with

$$\mathcal{L}_{stiff} = \frac{\left\| \mathbf{C}_s^{\text{DNS}} - \mathcal{DMN}(\mathbf{C}_s^{p1}, \mathbf{C}_s^{p2}, \hat{z}, \hat{\alpha}, \hat{\beta}, \hat{\gamma}) \right\|^2}{\left\| \mathbf{C}_s^{\text{DNS}} \right\|^2} \quad (19)$$

Here, λ is a hyperparameter, and s denotes the index of a training sample. During training, the dataset is partitioned into mini-batches, and the trainable parameters are optimized using stochastic gradient descent (SGD)[23].

The forward propagation of the DMN homogenization process is as follows. Initially, the stiffness matrices are assigned to the bottom-layer nodes according to:

$$\mathbf{C}_N^k = \begin{cases} \mathbf{C}^{p1}, & k = 1, 3, \dots, 2^N - 1 \\ \mathbf{C}^{p2}, & k = 2, 4, \dots, 2^N \end{cases}. \quad (20)$$

Starting from the bottom layer, the homogenization process propagates through the hierarchical building blocks layer by layer, applying Eq.(8) for *stiffness homogenization* and Eq.(14) for *rotation* at each building block. Ultimately, the homogenized stiffness at the root node, $\bar{\mathbf{C}}_1^1$, corresponds to the homogenized stiffness matrix of the RVE:

$$\mathbf{C}^{\text{DMN}} = \bar{\mathbf{C}}_1^1. \quad (21)$$

2.4 Online prediction

Online prediction extends the trained DMN to nonlinear regimes by introducing residual strain at each bottom node \mathcal{B}_N^j ($j = 1, \dots, 2^{N-1}$). Each bottom node functions as an independent material unit, characterized by its strain $\boldsymbol{\varepsilon}_N^j$, stress $\boldsymbol{\sigma}_N^j$, internal variables $\boldsymbol{\beta}_N^j$, and residual strain $\delta\boldsymbol{\varepsilon}_N^j$.

At the root node \mathcal{B}_1^1 , the stress-strain relationship is given by:

$$\Delta\boldsymbol{\varepsilon}^{\text{DMN}} = \mathbf{C}^{\text{DMN}^{-1}} \Delta\boldsymbol{\sigma}^{\text{DMN}} + \delta\boldsymbol{\varepsilon}^{\text{DMN}}. \quad (22)$$

Given a macroscopic loading condition, the goal of DMN is to ensure equilibrium between the bottom node responses and the applied loading. This is achieved

through Newton's method, which iteratively solves the nonlinear DMN system via two processes: homogenization and de-homogenization, as shown in Fig. 3.

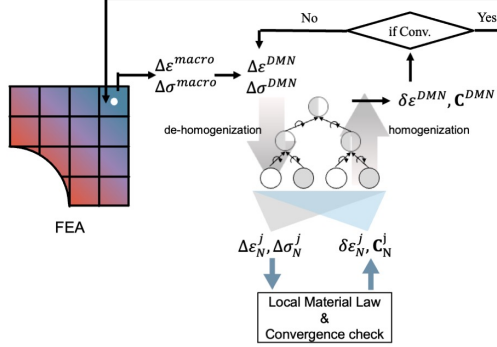


Fig. 3 Schematic representation of DMN in the online prediction phase.

During homogenization, the residual strain $\delta \epsilon^{DMN}$ and the homogenized stiffness matrix \mathbf{C}^{DMN} are computed by aggregating information from the bottom nodes to the root node. Based on the macroscopic loading condition, the overall incremental strain $\Delta \epsilon^{DMN}$ and stress $\Delta \sigma^{DMN}$ are then determined.

In the de-homogenization step, $\Delta \epsilon^{DMN}$ and $\Delta \sigma^{DMN}$ propagate back to the bottom nodes, where the local material law is evaluated. At each iteration i , the bottom node strains update as $\Delta \epsilon_N^{j, iter=i}$. Convergence is reached when the relative difference between $\Delta \epsilon_N^{j, iter=i}$ and $\Delta \epsilon_N^{j, iter=i-1}$ falls below a predefined threshold; otherwise, the updated strain continues in the next iteration.

At bottom layer N , each bottom node \mathcal{B}_N^j ($j = 1, \dots, 2^{N-1}$) receives an incremental strain $\Delta \epsilon_N^j$. At this stage, the bottom nodes need to satisfy the local material law:

$$\Delta \sigma_N^j = \Delta \sigma_N^j(\Delta \epsilon_N^j, \epsilon_N^j, \sigma_N^j, \beta_N^j) \quad (23)$$

and

$$\mathbf{C}_N^j = \mathbf{C}_N^j(\Delta \epsilon_N^j, \epsilon_N^j, \sigma_N^j, \beta_N^j) \quad (24)$$

From these expressions, both $\Delta \sigma_N^j$ and \mathbf{C}_N^j are determined. The corresponding stress-strain relationship at the bottom node is:

$$\delta \epsilon_N^j = \Delta \epsilon_N^j - \mathbf{D}_N^j \Delta \sigma_N^j \quad (25)$$

where \mathbf{D}_N^j is the compliance matrix, the inverse of the stiffness matrix \mathbf{C}_N^j .

The computed residual strain $\delta\epsilon_N^j$ and stiffness matrix \mathbf{C}_N^j at the bottom nodes are then homogenized to the root node \mathcal{B}_1^1 . The homogenization of the stiffness matrix follows Eq.(8) and Eq.(14).

Similarly, the residual strain undergoes an intermediate homogenization step, followed by a rotation operation, with updates applied layer by layer. The intermediate homogenized residual strain is computed as:

$$\begin{aligned} \delta\epsilon = f_1\delta\epsilon^1 + f_2\delta\epsilon^2 + \\ f_1f_2 \left(\begin{bmatrix} D_{11}^1 & D_{12}^1 & D_{16}^1 \\ D_{21}^1 & D_{22}^1 & D_{26}^1 \\ D_{31}^1 & D_{32}^1 & D_{36}^1 \\ D_{41}^1 & D_{42}^1 & D_{46}^1 \\ D_{51}^1 & D_{52}^1 & D_{56}^1 \\ D_{61}^1 & D_{62}^1 & D_{66}^1 \end{bmatrix} - \begin{bmatrix} D_{11}^2 & D_{12}^2 & D_{16}^2 \\ D_{21}^2 & D_{22}^2 & D_{26}^2 \\ D_{31}^2 & D_{32}^2 & D_{36}^2 \\ D_{41}^2 & D_{42}^2 & D_{46}^2 \\ D_{51}^2 & D_{52}^2 & D_{56}^2 \\ D_{61}^2 & D_{62}^2 & D_{66}^2 \end{bmatrix} \right) \\ \left[\begin{matrix} f_1D_{11}^2 + f_2D_{11}^1 & f_1D_{12}^2 + f_2D_{12}^1 & f_1D_{16}^2 + f_2D_{16}^1 \\ f_1D_{21}^2 + f_2D_{21}^1 & f_1D_{22}^2 + f_2D_{22}^1 & f_1D_{26}^2 + f_2D_{26}^1 \\ f_1D_{61}^2 + f_2D_{61}^1 & f_1D_{62}^2 + f_2D_{62}^1 & f_1D_{66}^2 + f_2D_{66}^1 \end{matrix} \right]^{-1} \begin{bmatrix} \delta\epsilon_1^2 - \delta\epsilon_1^1 \\ \delta\epsilon_2^2 - \delta\epsilon_2^1 \\ \delta\epsilon_6^2 - \delta\epsilon_6^1 \end{bmatrix} \end{aligned} \quad (26)$$

where superscripts ¹, ² denote phase 1 and phase 2, while subscripts indicate the compliance matrix indices or vector components.

The rotated residual strain is then computed as:

$$\delta\bar{\epsilon} = \mathbf{R}(\alpha, \beta, \gamma)\delta\epsilon \quad (27)$$

2.5 Rationale beyond the DMNs

The success of DMNs stems from their physics-informed architecture, which inherently enforces thermodynamic consistency and material stability. Unlike purely data-driven neural networks that infer constitutive laws from empirical data, DMNs embed fundamental physical principles directly into their network topology. This intrinsic design ensures essential conditions—such as monotonic stress-strain behavior, positive energy dissipation, and stable material evolution—without requiring additional penalty terms or constraints [21].

Several key factors enable DMNs to maintain robust physical consistency and strong performance beyond their training domain [21]:

- **Monotonic stress-strain response:** Each DMN building block is derived from interfacial equilibrium conditions. If the constituent materials at the lowest hierarchical level exhibit monotonic stress-strain behavior, the overall DMN response remains monotonic. This prevents artificial softening or non-physical instabilities, ensuring numerical stability and realistic material behavior.
- **Convexity and stability of the energy:** The free energy of each DMN building block is expressed as a weighted combination of the free energies of its constituent

phases. This construction preserves convexity in the global energy function, ensuring a unique and physically valid constitutive response while mitigating the risk of numerical failure in simulations.

- **Inherited dissipation inequality:** DMNs inherently satisfy the second law of thermodynamics by design. As each constituent phase enforces non-negative energy dissipation, the overall DMN ensures that any inelastic deformation results in a net positive (or zero) dissipated energy, preventing artificial energy generation.
- **Intrinsic enforcement of physics:** Instead of imposing external constraints or penalty terms, such as incorporating governing equations into the loss function, which may still lead to inaccuracies when extrapolating far beyond the training domain, DMNs embed thermodynamic laws directly within their hierarchical topology. This inductive bias inherently enforces equilibrium, stability, and dissipation constraints within entire network, ensuring thermodynamic consistency even under conditions well beyond the training data.

Overall, DMNs effectively address multiscale and nonlinear material problems by leveraging a robust physical foundation at every building block. This built-in physics enforcement guarantees monotonicity, stable energy evolution, and nonnegative dissipation. As a result, DMNs not only produce reliable predictions within the trained domain (interpolation) but also exhibit exceptional extrapolation capabilities.

3 Current Directions

3.1 Advancements in DMN methodologies

Recent advancements in DMN methodologies have significantly enhanced their computational efficiency, physical interpretability, and applicability across diverse material systems. Table 1 provides an overview of key developments in DMN-based models, highlighting their primary objectives and relevant references.

Table 1 Recent advancements in DMN-based models and their objectives.

Model	Key Objective	Reference
Rotation-free DMN	Extend DMN to multiphase materials and eliminate rotational DOFs ¹	[21]
IMN	Extend DMN to porous materials with enforced Hill-Mandel condition	[24, 25]
ODMN	Extend DMN to polycrystalline materials with texture evolution	[26]
MIpDMN	Extend DMN to incorporate thermal (conductivity & expansion) effects	[27]
Thermomechanical DMN	Extend DMN to incorporate thermal (expansion) effects	[28]
Thermal DMN	Extend DMN to incorporate thermal (conductivity) effects	[29]
DMN with Damage Effect	Extend DMN to integrate cohesive networks for damage modeling	[30, 31]
FDMN	Extend DMN to model non-Newtonian fluid dynamics	[32]

¹DOFs: degrees of freedoms

3.1.1 Rotation-free DMN

Gajek et al. extended the DMN framework by identifying that rotational DOFs at the bottom nodes of undirected composite materials are redundant [21]. Their analysis, based on Volterra series approximations and multiple-input multiple-output (MIMO) dynamical system frameworks, demonstrated that these DOFs have negligible influence on the overall material response.

By eliminating these unnecessary DOFs, the rotation-free DMN significantly improves computational efficiency while maintaining predictive accuracy. Furthermore, this streamlined formulation naturally extends to multiphase materials, making it a scalable and versatile framework for modeling complex microstructures [21].

3.1.2 Interaction-based material network

Building upon the rotation-free DMN, Van Dung Nguyen and Ludovic Noels introduced the interaction-based material network (IMN) to extend DMN’s applicability to porous materials [24, 25].

IMN reformulates DMN by explicitly distinguishing material nodes from the material network, as shown in Fig. 4. In this framework, the bottom nodes of DMN are treated as independent material nodes, while the remaining hierarchical structure constitutes the material network, where each tree node represents an interaction mechanism. An IMN consists of N material nodes and M tree nodes, which can be interpreted as modeling an RVE with N independent material units, grouped into M interaction sets, each of which must satisfy the Hill-Mandel condition. Each interaction mechanism within the material network is characterized by:

- An interaction direction \mathbf{G}^j , corresponding to the force-equilibrium direction.
- An interaction incompatibility \mathbf{a}^j , representing deformation fluctuations.

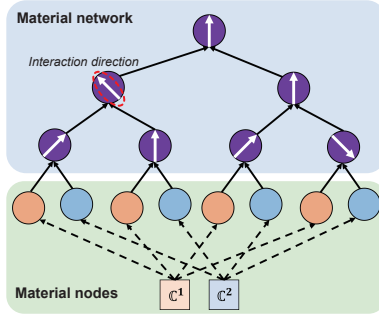


Fig. 4 Schematic illustration of the IMN framework, which consists of a material network and a set of material nodes.

A key component of IMN during online prediction is its interaction mapping, which governs the deformation gradient distribution across material nodes. This mapping is

defined as

$$\mathbf{F}^i = \bar{\mathbf{F}} + \sum_{j=0}^M \alpha^{i,j} \mathbf{a}^j \otimes \mathbf{G}^j, \quad \text{for } i = 0, 1, \dots, N-1 \quad (28)$$

where i indexes the material nodes, and j indexes the interaction mechanisms. From Eq. (28), the fluctuation part of the deformation gradient is decomposed into M interaction modes, each governed by a specific interaction mechanism represented by $\mathbf{a}^j \otimes \mathbf{G}^j$.

Beyond its theoretical foundation, IMN introduces a significant computational advantage over traditional DMN. Unlike DMN, which requires layer-by-layer reconstruction during online prediction, IMN's interaction mapping reformulates dehomogenization as a matrix operation, significantly improving computational efficiency. Studies have demonstrated that IMN achieves substantial speedup in both offline training and online prediction [33].

3.1.3 Orientation-aware interaction-based DMN

Building upon the IMN framework, recent studies have introduced the orientation-aware interaction-based DMN (ODMN), which incorporates an orientation-aware mechanism at the material nodes, making it applicable to multiphase polycrystalline material systems [26], as shown in Fig. 5. This mechanism introduces three trainable parameters at each material node: the Tait-Bryan angles α , β , and γ . These angles define a set of elementary rotation matrices, which collectively govern the rotation of each material node.

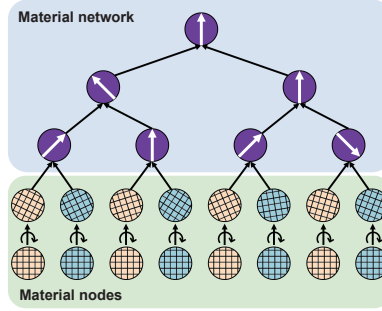


Fig. 5 Schematic illustration of the ODMN framework. Each material node is associated with trainable rotation angles, encoding local orientation information within the RVE.

During online prediction, the rotation matrix \mathbf{R}^i for a material node index i is constructed using the trainable angles as follows:

$$\mathbf{R}^i = \begin{bmatrix} 1 & 0 & 0 \\ 0 & \cos \alpha^i & -\sin \alpha^i \\ 0 & \sin \alpha^i & \cos \alpha^i \end{bmatrix} \begin{bmatrix} \cos \beta^i & 0 & \sin \beta^i \\ 0 & 1 & 0 \\ -\sin \beta^i & 0 & \cos \beta^i \end{bmatrix} \begin{bmatrix} \cos \gamma^i & -\sin \gamma^i & 0 \\ \sin \gamma^i & \cos \gamma^i & 0 \\ 0 & 0 & 1 \end{bmatrix} \quad (29)$$

At the initial loading state ($t = 0$), the elastic and plastic deformation gradients are initialized as:

$$\mathbf{F}_e^i(t = 0) = \mathbf{R}^i, \quad \mathbf{F}_p^i(t = 0) = \mathbf{R}^{i-1} \quad (30)$$

For $t > 0$, the updated rotation matrix \mathbf{R}_t^i at material node i can be obtained via the polar decomposition of the elastic deformation gradient:

$$\mathbf{F}_e^i(t > 0) = \mathbf{R}_t^i \mathbf{U}_t^i \quad (31)$$

The extracted rotation matrix \mathbf{R}_t^i and w^i are then used to reconstruct the orientation distribution function (ODF), enabling the characterization of crystallographic texture evolution.

While the original DMN can be applied to polycrystalline materials, a key limitation arises from the entanglement of bottom node rotation angles with the rotation angles of hierarchical building blocks within the homogenization function. In the original DMN, each building block is assumed to rotate throughout both homogenization and de-homogenization. Consequently, any change in the bottom node rotation disrupts the force-equilibrium condition of the DMN, leading to simulation instability and non-convergence during online prediction.

In contrast, ODMN decouples material rotation from building block rotations. Rotation does not occur in the building blocks; rather, force-equilibrium directions are established. This distinction eliminates the need for rotation-related operations during both homogenization and de-homogenization in online prediction. As a result, ODMN allows material nodes to undergo deformation-induced rigid-body rotation while preserving the Hill-Mandel condition, thereby enabling texture evolution prediction in polycrystalline materials.

3.1.4 Micromechanics-informed parametric DMN

The DMN framework has been further extended to incorporate anisotropic thermal conductivity and thermal expansion in the micromechanics-informed parametric DMN (MIpDMN) [27]. In the original DMN building block, the laminate homogenization function for stiffness is expressed as:

$$\bar{\mathbf{C}} = \text{Lam}_{\mathbf{C}}(\mathbf{C}^{p1}, \mathbf{C}^{p2}). \quad (32)$$

Similarly, the effective thermal conductivity \bar{k} follows:

$$\bar{k} = \text{Lam}_k(k^{p1}, k^{p2}). \quad (33)$$

The laminate thermal homogenization function is governed by Fourier's law:

$$\vec{q} = -k \nabla T. \quad (34)$$

To derive the effective thermal conductivity, the heat flux \vec{q} and the temperature gradient ∇T are decomposed into their tangential and normal components, denoted by

superscripts t and n , respectively. At the interface, the continuity conditions impose:

$$\begin{bmatrix} \nabla T_2^t \\ \bar{q}_1^n \end{bmatrix} = \begin{bmatrix} \nabla T_2^t \\ \bar{q}_2^n \end{bmatrix} \quad (35)$$

By solving for the effective thermal conductivity, we obtain:

$$\bar{k} = f^1(k_1 - k_2)\mathbf{A} + k_2, \quad \mathbf{A} = \tilde{k}^{-1}\tilde{k}_2, \quad \tilde{k} = (1 - f^1)\tilde{k}_1 + f^1\tilde{k}_2 \quad (36)$$

where

$$\tilde{k}_\alpha = \begin{bmatrix} \mathbb{I}_{2 \times 2} & \mathbf{0}_{2 \times 1} \\ k_\alpha^{nt} & k_\alpha^{nn} \end{bmatrix}, \quad \alpha = 1, 2 \quad (37)$$

Beyond thermal conductivity, MIpDMN also incorporates effective stiffness homogenization while accounting for thermal expansion. The corresponding laminate homogenization function is expressed as:

$$(\bar{\mathbf{C}}, \bar{\alpha}) = \text{Lam}_{\mathbb{C}, \alpha}(\mathbf{C}^{p1}, \mathbf{C}^{p2}, \alpha_1, \alpha_2). \quad (38)$$

Assuming a uniform temperature difference ΔT and a traction vector $\bar{\sigma} \cdot \bar{n}$ on the RVE boundary, the thermoelastic constitutive equation yields:

$$\varepsilon_1 = \varepsilon_2 = \mathbb{S}_1 \bar{\sigma} + \alpha_1 \Delta T = \mathbb{S}_2 \bar{\sigma} + \alpha_2 \Delta T \quad (39)$$

where \mathbb{S}_1 and \mathbb{S}_2 represent the compliance matrices of phases 1 and 2, respectively.

By further derivation, the effective thermal expansion coefficient is given by:

$$\bar{\alpha} = \alpha_1 + (\bar{\mathbb{S}} - \mathbb{S}_1)(\mathbb{S}_1 - \mathbb{S}_2)^{-1}(\alpha_1 - \alpha_2). \quad (40)$$

Furthermore, MIpDMN enhances the adaptability of DMN to various microstructures, as demonstrated in a later section. To validate the proposed MIpDMN framework, an analysis was conducted on its predictions of effective thermal conductivity and the effective coefficient of thermal expansion in ellipsoidal inclusion composites, considering varying fiber volume fractions and aspect ratios. The results confirm that MIpDMN accurately predicts both effective thermal conductivity and the effective coefficient of thermal expansion across different microstructures.

3.1.5 Thermomechanical DMN

Building upon the isothermal DMN framework [21, 24, 34], Shin et al. [28] extended the methodology to thermomechanical problems by incorporating thermal expansion effects while ensuring energy conservation. This extension is achieved by enforcing interface traction continuity within each building block and modifying the Hill–Mandel condition to account for temperature gradients, as shown in Fig. 6.

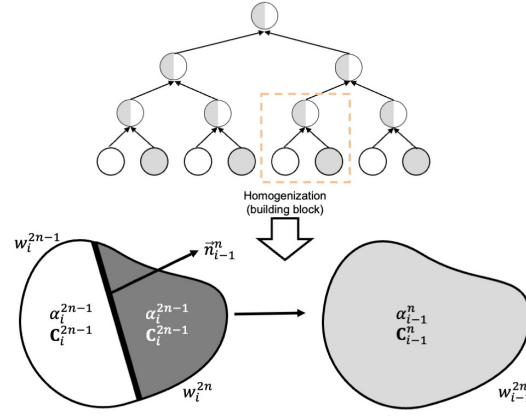


Fig. 6 Schematic illustration of thermomechanical DMN framework.

For each building block, the continuity of interface traction is given by

$$\mathbf{H}_h^\top (\boldsymbol{\sigma}_1 - \boldsymbol{\sigma}_2) = \mathbf{0}, \quad (41)$$

where \mathbf{H}_h^\top is a 3×6 matrix associated with the interface normal direction. The homogenized strain and stress satisfy the averaging theorem:

$$\bar{\boldsymbol{\varepsilon}} = f_1 \boldsymbol{\varepsilon}_1 + f_2 \boldsymbol{\varepsilon}_2, \quad \bar{\boldsymbol{\sigma}} = f_1 \boldsymbol{\sigma}_1 + f_2 \boldsymbol{\sigma}_2, \quad (42)$$

where f_1 and f_2 are the volume fractions of the two phases. To incorporate thermal effects, the Hill–Mandel condition is extended following Levin’s theorem:

$$(\bar{\boldsymbol{\varepsilon}} - \bar{\boldsymbol{\alpha}} \Delta T)^\top \bar{\boldsymbol{\sigma}} = f_1 (\boldsymbol{\varepsilon}_1 - \boldsymbol{\alpha}_1 \Delta T)^\top \boldsymbol{\sigma}_1 + f_2 (\boldsymbol{\varepsilon}_2 - \boldsymbol{\alpha}_2 \Delta T)^\top \boldsymbol{\sigma}_2. \quad (43)$$

Rearranging Eq. (43) yields

$$f_1 f_2 (\boldsymbol{\varepsilon}_1 - \boldsymbol{\varepsilon}_2)^\top (\boldsymbol{\sigma}_1 - \boldsymbol{\sigma}_2) = \left[f_1 (\boldsymbol{\alpha}_1 - \bar{\boldsymbol{\alpha}})^\top \boldsymbol{\sigma}_1 + f_2 (\boldsymbol{\alpha}_2 - \bar{\boldsymbol{\alpha}})^\top \boldsymbol{\sigma}_2 \right] \Delta T. \quad (44)$$

The homogenization problem can be divided into two subproblems: one under isothermal conditions (ΔT) with a homogeneous traction boundary condition, and the other accounting for traction-free thermal variations.

Under isothermal conditions ($\Delta T = 0$), Eq. (44) simplifies to

$$f_1 f_2 (\boldsymbol{\varepsilon}_1 - \boldsymbol{\varepsilon}_2)^\top (\boldsymbol{\sigma}_1 - \boldsymbol{\sigma}_2) = 0. \quad (45)$$

Using Eq.(41), this leads to

$$\begin{aligned}
(\boldsymbol{\varepsilon}_1 - \boldsymbol{\varepsilon}_2)^\top &= \frac{1}{f_1 f_2} (\mathbf{H} \mathbf{b})^\top, \\
\boldsymbol{\varepsilon}_1 &= \bar{\boldsymbol{\varepsilon}} + \frac{\mathbf{H} \mathbf{b}}{f_1}, \\
\boldsymbol{\varepsilon}_2 &= \bar{\boldsymbol{\varepsilon}} - \frac{\mathbf{H} \mathbf{b}}{f_2},
\end{aligned} \tag{46}$$

where \mathbf{b} is an arbitrary vector, and $\bar{\boldsymbol{\varepsilon}}$ is the homogenized strain.

In the presence of a temperature variation, Eq. (44) simplifies to

$$f_1(\boldsymbol{\alpha}_1 - \bar{\boldsymbol{\alpha}})^\top \boldsymbol{\sigma}_1 + f_2(\boldsymbol{\alpha}_2 - \bar{\boldsymbol{\alpha}})^\top \boldsymbol{\sigma}_2 = 0, \tag{47}$$

where ΔT can take an arbitrary value. Using Eqs.(46) and (47), the linear homogenization within each building block is given by

$$\bar{\mathbf{C}} = f_1 \mathbf{C}_1 + f_2 \mathbf{C}_2 + (\mathbf{C}_1 - \mathbf{C}_2) \mathbf{H} \mathbf{X}_1, \tag{48}$$

$$\bar{\boldsymbol{\alpha}} = \bar{\mathbf{C}}^{-1} \left[(\mathbf{C}_2 - \mathbf{C}_1) \mathbf{H} \mathbf{X}_2 + f_1 \mathbf{C}_1 \boldsymbol{\alpha}_1 + f_2 \mathbf{C}_2 \boldsymbol{\alpha}_2 \right], \tag{49}$$

where the \mathbf{X}_1 and \mathbf{X}_2 are analytical functions of $(\mathbf{C}_1, \mathbf{C}_2, \alpha_1, \alpha_2, f_1, f_2)$.

Finally, the thermomechanical DMN was validated through thermo-elastic-viscoplastic simulations, where mechanical boundary conditions were applied while temperature variations were progressively introduced. The results confirmed that the model accurately captures the coupled mechanical and thermal responses of heterogeneous materials, demonstrating its effectiveness in thermomechanical analysis.

3.1.6 Thermal DMN

Dongil Shin et al. proposed the thermal DMN to model thermal conductivity in woven composite materials [29]. This framework explicitly incorporates both the heat flux \mathbf{q} and the temperature gradient $\psi = -\nabla T$ into the building block formulation, enabling an accurate representation of thermal transport in anisotropic and heterogeneous materials, as shown in Fig. 7.

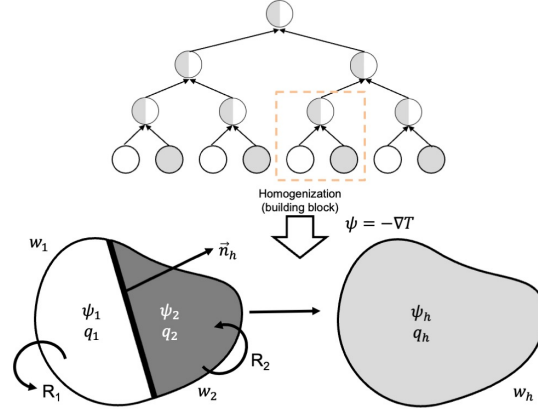


Fig. 7 Schematic illustration of thermal DMN framework.

Within each building block, the heat flux vectors for phase 1, phase 2, and the homogenized response are denoted as \mathbf{q}_1 , \mathbf{q}_2 , and \mathbf{q}_h , respectively, while the corresponding temperature gradient vectors are ψ_1 , ψ_2 , and ψ_h . The formulation is governed by the following conditions:

- Entropy convergence condition:

$$\psi_1 - \psi_2 = \zeta \vec{n}_h / (f^1 f^2) \quad (50)$$

where \vec{n}_h represents the interface direction between the two phases.

- Homogenization of field variables:

$$\psi_h = f^1 \psi_1 + f^2 \psi_2 \quad (51)$$

$$\mathbf{q}_h = f^1 \mathbf{q}_1 + f^2 \mathbf{q}_2 \quad (52)$$

- Heat flux continuity condition:

$$\vec{n}_h^\top (\mathbf{q}_2 - \mathbf{q}_1) = 0 \quad (53)$$

- Constitutive relations:

$$\mathbf{q}_1 = \mathbf{R}_1^\top \mathbf{k}_1 \mathbf{R}_1 \psi_1 \quad (54)$$

$$\mathbf{q}_2 = \mathbf{R}_2^\top \mathbf{k}_2 \mathbf{R}_2 \psi_2 \quad (55)$$

$$\mathbf{q}_h = \mathbf{k}_h \psi_h \quad (56)$$

where \mathbf{R}_1 and \mathbf{R}_2 are the trainable rotation matrices associated with the child nodes, allowing the model to capture the anisotropic characteristics of the thermal conductivity tensor adaptively.

Each building block consists of 19 variables, including \mathbf{q}_1 , \mathbf{q}_2 , \mathbf{q}_h , ψ_1 , ψ_2 , ψ_h , and ζ . These variables are constrained by 19 equations, given in Eqs. (50)–(56), enabling the derivation of an analytical homogenization function for thermal conductivity.

Furthermore, the nodal rotation mechanism in thermal DMN enhances its ability to represent directional heat conduction, improving the accuracy of thermal behavior modeling in complex woven composites.

3.1.7 DMN with damage effect

To model the progressive degradation of materials, the DMN framework can be extended to incorporate interfacial failure and debonding. This is achieved by enriching specific bottom nodes of the DMN and associated them with dedicated cohesive networks. Each cohesive network consists of multiple cohesive layers designed to capture interfacial behavior, as illustrated in Fig. 8 [30, 31].

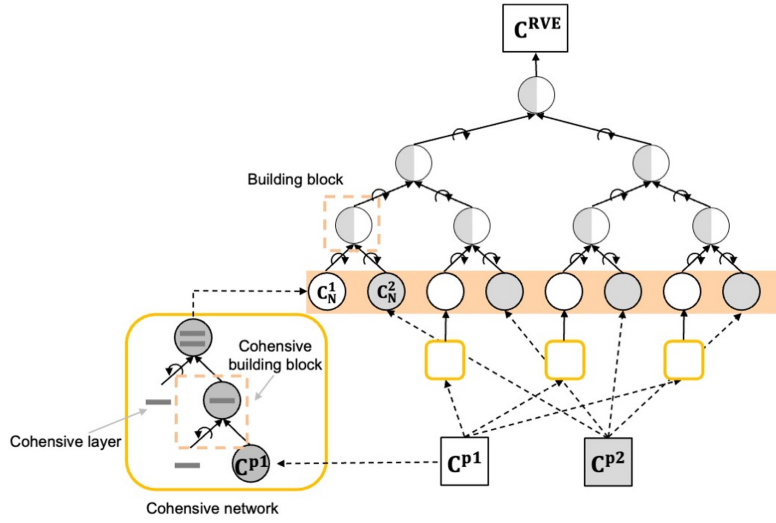


Fig. 8 Schematic illustration of the cohesive network integration within DMN.

For each enriched node q , the cohesive layers indexed by p , are sequentially embedded within the base material through cohesive building blocks. To maintain material consistency, the base material in the cohesive network must represent the same microscale constituent as the one originally present in the bottom layer of the DMN. Each enriched node q is associated with a distinct cohesive network, parameterized by a set of trainable variables: $\{\tilde{z}_q^p, \tilde{\alpha}_q^p, \tilde{\beta}_q^p, \tilde{\gamma}_q^p\}$. Additionally, a reciprocal length parameter $\tilde{\nu}$ is introduced to account for the size effects of the interface, defined as:

$$\tilde{\nu}_q^p = \frac{\max(\tilde{z}_q^p, 0)}{L} \quad (57)$$

where L is the characteristic length of the RVE.

The traction-separation law governs the response of the cohesive layers and is expressed as:

$$\Delta d = G\Delta t + \delta d, \quad (58)$$

where:

1. Δd represents the incremental separation displacement,
2. Δt represents the incremental separation force,
3. G is the cohesive layer stiffness matrix,
4. δd is the residual displacement vector.

Thus, the homogenized compliance matrix of the cohesive building block can be analytically derived as:

$$D = D(D^0, G, \tilde{z}, \tilde{\alpha}, \tilde{\beta}, \tilde{\gamma}), \quad (59)$$

along with the residual strain formulation:

$$\delta \varepsilon = \delta \varepsilon(\delta \varepsilon^0, \delta d, \tilde{z}, \tilde{\alpha}, \tilde{\beta}, \tilde{\gamma}). \quad (60)$$

Here, D^0 and D denote the compliance matrices before and after homogenization, respectively. The parameters $\tilde{z}, \tilde{\alpha}, \tilde{\beta}, \tilde{\gamma}$ are trainable, while $\delta \varepsilon^0$ and $\delta \varepsilon$ represent the residual strain variables before and after homogenization.

The training process for the DMN with cohesive layers follows a two-stage approach. In the first stage, the DMN is trained independently without incorporating the cohesive network. In the second stage, the cohesive network is integrated while retaining the previously trained DMN parameters. The fully trained model, initially developed using elastic data, can then be extended to capture nonlinear material behavior.

3.1.8 Flexible DMN

The Flexible DMN (FDMN) extends the standard DMN framework to model suspensions of rigid fibers in a non-Newtonian fluid [32]. A closed-form solution for two-layer linear homogenization is derived, establishing a theoretical foundation for this approach. By incorporating the rheological behavior of the surrounding medium, FDMN effectively predicts the effective stress response of shear-thinning fiber suspensions embedded in a Cross-type matrix material across a wide range of shear rates and under various loading conditions. This formulation enables accurate modeling of the complex interplay between fiber rigidity and non-Newtonian fluid behavior in heterogeneous materials.

3.2 Generalizing DMNs to diverse microstructures

The original DMN framework has a fundamental limitation: a single DMN is typically trained for a specific microstructure. If the microstructure changes, the model requires retraining, which is impractical for industrial applications where microstructural variations are common. To address this challenge, several studies have explored methods

to extend DMNs for handling diverse microstructures without the need for complete retraining. These advancements focus on integrating microstructural descriptors, adaptive training strategies, and transferable representations to enhance model generalization. Table 2 summarizes key developments in this area, highlighting different approaches to improving DMN adaptability across varying microstructures.

Table 2 DMN-based models for handling diverse microstructures.

Study	Method	Microstructure	Ref
Transfer Learning DMN	Linear Interpolation	Circular Inclusions	[35]
MgDMN	Linear Interpolation	3D SFRP ¹	[36]
MIpDMN	Linear Interpolation	Circular Inclusions	[27]
GNN-DMN	GNN	Short Fibers	[37]
FM-IMN	FM	Short Fibers	[38]

¹SFRP: Short Fiber Reinforced Polymer.

3.2.1 Simple interpolation

A straightforward approach to adapting a pre-trained DMN for new microstructures involves parameter interpolation [35]. Since the trainable weights in the DMN reflect the volume fraction of the material phases, the model can be adjusted for a new microstructure by rescaling its parameters. Consider a pre-trained DMN with a phase 2 volume fraction vf_2^{trained} , while an unseen RVE has a different but known volume fraction vf_2^{new} . The parameters at the bottom node indexed by j are given by:

$$z_{\text{unseen}}^j = \begin{cases} \frac{1-vf_2^{\text{new}}}{1-vf_2^{\text{trained}}} \text{ReLu}(z_{\text{trained}}^j), & \text{if } j \text{ is odd,} \\ \frac{vf_2^{\text{new}}}{vf_2^{\text{trained}}} \text{ReLu}(z_{\text{trained}}^j), & \text{if } j \text{ is even.} \end{cases} \quad (61)$$

The trainable rotation angles for each building block remain unchanged:

$$\begin{cases} \alpha_{i,\text{unseen}}^k = \alpha_{i,\text{trained}}^k, \\ \beta_{i,\text{unseen}}^k = \beta_{i,\text{trained}}^k, \\ \gamma_{i,\text{unseen}}^k = \gamma_{i,\text{trained}}^k. \end{cases} \quad (62)$$

This approach eliminates the need for additional training and allows for efficient adaptation to new microstructures. However, its accuracy is inherently limited.

3.2.2 Transfer learning

To improve upon interpolation-based adaptation, transfer learning has been explored as a means of extending DMNs to new microstructures while reducing the need for full retraining [35].

In this approach, a dataset is first generated with multiple predefined volume fractions (e.g., $vf_2 = 0.1, 0.2, \dots, 0.6$), and corresponding DMN models are trained. If an unseen RVE has a volume fraction vf_2^{new} that falls within the range $[vf_2^{\text{low}}, vf_2^{\text{high}}]$, its DMN parameters are interpolated from the nearest pre-trained models as

$$z_{\text{unseen}}^j = \rho \text{ReLu}(z_{\text{low}}^j) + (1 - \rho) \text{ReLu}(z_{\text{high}}^j) \quad (63)$$

where the interpolation coefficient ρ is defined as:

$$\rho = \frac{vf_2^{\text{high}} - vf_2^{\text{new}}}{vf_2^{\text{high}} - vf_2^{\text{low}}}. \quad (64)$$

Similarly, the trainable rotation angles at depth i and index k are interpolated as:

$$\begin{cases} \alpha_{i,\text{unseen}}^k = \rho \alpha_{i,\text{low}}^k + (1 - \rho) \alpha_{i,\text{high}}^k, \\ \beta_{i,\text{unseen}}^k = \rho \beta_{i,\text{low}}^k + (1 - \rho) \beta_{i,\text{high}}^k, \\ \gamma_{i,\text{unseen}}^k = \rho \gamma_{i,\text{low}}^k + (1 - \rho) \gamma_{i,\text{high}}^k. \end{cases} \quad (65)$$

This transfer learning-based interpolation strategy allows DMNs to generalize to new microstructures more effectively than simple interpolation by leveraging a broader

range of pre-trained models. By integrating knowledge from multiple microstructures, this approach mitigates errors arising from simple parameter scaling and provides more accurate predictions across a diverse range of material configurations.

3.2.3 Microstructure-guided DMN

For complex RVE geometries, such as SFRP, the microstructure-guided DMN (MgDMN) extends the standard DMN framework by introducing a parameterization of the microstructure space [36]. This enhancement enables MgDMN to capture critical microstructural features and generalize across a broad range of microstructures, as shown in Fig. 9. Unlike traditional DMNs that must be retrained for every new microstructure, MgDMN employs an interpolation scheme to infer DMN parameters using only a few pre-trained DMNs.

In MgDMN, the DMN homogenization process considers both the volume fraction (VF) and the orientation state. For a building block \mathcal{B}_i^k at layer i and index k , the VF (denoted by VF_i^k) is defined as:

$$\text{VF}_i^k = f^1 \text{VF}_{i+1}^{2k-1} + f^2 \text{VF}_{i+1}^{2k} \quad (66)$$

where VF_i^k is the actual volume fraction of phase 1, and f^1 and f^2 are the weight proportions of the child building blocks (computed via Eq. (7)).

The orientation state is aggregated based on the dyadic product of a directional vector \vec{p} . The second-order orientation tensor $A = [a_{ij}]$ is given by [39]:

$$a_{ij} = \int p_i \otimes p_j \Phi(\vec{p}) d\vec{p}. \quad (67)$$

where $\Phi(\vec{p})$ is the probability density function describing the orientation distribution.

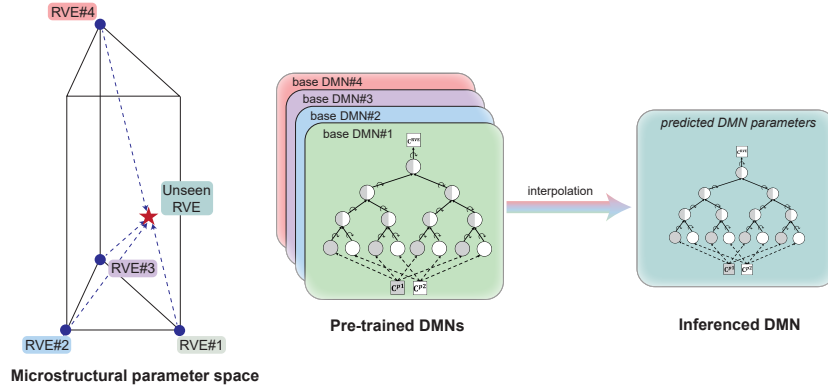


Fig. 9 Schematic illustration of the microstructural parameter space. The DMN parameters for an unseen RVE are obtained by interpolating four base pre-trained DMNs in this space.

Within this framework, the microstructure is characterized by the VF and orientation tensors. After considering rotational symmetries, the parameter space can be reduced further. In general, for an N_p -phase microstructure, $6N_p - 8$ distinct microstructures are required to span the microstructural parameter space fully. In the special case of a two-phase SFRP, four distinct microstructures suffice to span the prism-shaped parameter space $\{\nu, a_{11}, a_{22}, a_{33}\}$.

These four microstructures correspond to:

1. Randomly oriented fibers at an $L\%$ fiber volume fraction,
2. Planar random fibers at an $L\%$ fiber volume fraction,
3. Aligned fibers at an $L\%$ fiber volume fraction,
4. Aligned fibers at an $H\%$ fiber volume fraction.

Here, L and H are set to 10% and 15%, respectively. Separate DMNs, referred to as the base DMNs, are trained on each of these four RVEs. For an unseen microstructure, interpolation is used to determine DMN parameters. Specifically, the unseen microstructure is projected into the parameter space to obtain $\{\tilde{\nu}, \tilde{a}_{11}, \tilde{a}_{22}, \tilde{a}_{33}\}$. The volume percentages $\{w_1, w_2, w_3, w_4\}$ associated with each base DMN are then computed by solving:

$$\begin{bmatrix} a_{11}^{(1)} & a_{11}^{(2)} & a_{11}^{(3)} & a_{11}^{(4)} \\ a_{22}^{(1)} & a_{22}^{(2)} & a_{22}^{(3)} & a_{22}^{(4)} \\ a_{33}^{(1)} & a_{33}^{(2)} & a_{33}^{(3)} & a_{33}^{(4)} \\ \nu^{(1)} & \nu^{(2)} & \nu^{(3)} & \nu^{(4)} \end{bmatrix} \begin{bmatrix} w^{(1)} \\ w^{(2)} \\ w^{(3)} \\ w^{(4)} \end{bmatrix} = \begin{bmatrix} \tilde{a}_{11} \\ \tilde{a}_{22} \\ \tilde{a}_{33} \\ \tilde{\nu} \end{bmatrix}. \quad (68)$$

Here, the superscript (i) represents the index of the base DMN microstructure parameters. Once these weights are determined, the DMN parameters $\tilde{\mathcal{P}}$ for the unseen microstructure are obtained as a weighted linear combination of the base DMNs:

$$\tilde{\mathcal{P}} = \sum_{i=1}^4 w^{(i)} \mathcal{P}^{(i)} \quad (69)$$

where \mathcal{P} represents DMN parameter (e.g., $z^{k=1, \dots, 2^{N-1}}$, $\alpha_{i=1, \dots, N}^{k=1, \dots, 2^{i-1}}$, $\beta_{i=1, \dots, N}^{k=1, \dots, 2^{i-1}}$, or $\gamma_{i=1, \dots, N}^{k=1, \dots, 2^{i-1}}$).

3.2.4 Micromechanics-informed parametric DMN

The micromechanics-informed parametric DMN (MIpDMN) incorporates micromechanical parameters to accommodate microstructural variations across different representative volume elements (RVEs) [27]. In MIpDMN, each microstructure is projected onto a parametric space \vec{p} , as shown in Fig. 10:

$$\vec{p} = \{v_f, \vec{q}\} \in \mathbb{R} \times \mathbb{R}^q \quad (70)$$

where v_f is the volume fraction, and \vec{q} represents morphological parameters orthogonal to v_f .

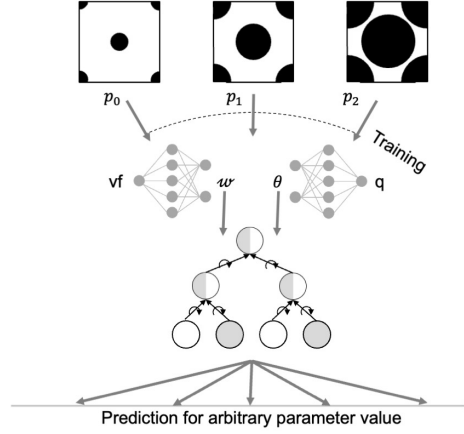


Fig. 10 Schematic illustration of the MIPDMN framework.

Since DMN parameters inherently encode microstructural characteristics, they can be expressed as functions of \vec{p} . Consequently, the overall homogenization process becomes:

$$(\vec{p}, \mathbf{C}^{p1}, \mathbf{C}^{p2}) \mapsto \bar{\mathbf{C}} \quad (71)$$

where \mathbf{C}^{p1} and \mathbf{C}^{p2} denote the phase stiffness matrices, and $\bar{\mathbf{C}}$ is the homogenized stiffness matrix.

The trainable DMN parameters can be classified into volume fraction-dependent parameters and rotation angles. In MIPDMN, the weight w is redefined as a linear function of volume fraction with the activation function σ :

$$w(\vec{p}) = w(v_f) = \sigma(W_1 \cdot v_f + W_0) \quad (72)$$

Similarly, the DMN rotation angles θ are modeled as a linear transformation of \vec{q} :

$$\theta(\vec{p}) = \theta(\vec{q}) = \text{ReLU}(\Theta_1 \cdot \vec{q} + \Theta_0) \quad (73)$$

where θ represents the set of rotation angles $\{\alpha, \beta, \gamma\}$ in the DMN.

In summary, the trainable parameters in MIPDMN related to the volume fraction consist of 2^{N+1} parameters, including w^j , W_1 , and W_0 . Meanwhile, the trainable parameters orthogonal to the volume fraction amount to $4 \times (q+1) \times (2^N - 1)$. For an unseen RVE, its microstructural representation is first mapped onto the parametric space \vec{p} , after which Eq.(72) and Eq.(73) are used to determine the corresponding MIPDMN parameters.

3.2.5 GNN-DMN framework

Recent advancements in DMNs have been achieved by integrating graph neural networks (GNNs) into the DMN framework, leading to the development of the GNN-DMN approach [37]. In GNN-DMN, the microstructure is discretized into a mesh, which is then used to construct a graph \mathbb{G} . Each mesh element is treated as a node, with mesh connectivity defining the graph edges. The node attributes include:

1. Area of mesh element
2. xy-coordinates of the element centroid
3. Phase of the mesh element
4. Boundary status of the element (whether it lies on the boundary)

These attributes are processed by a GNN to extract a latent vector X_{feat} , which is subsequently transformed into the DMN parameters \vec{p} via a fully connected network. The homogenization process in GNN-DMN is formulated as:

$$(\vec{p}(\mathbb{G}), \mathbf{C}^{p1}, \mathbf{C}^{p2}) \mapsto \bar{\mathbf{C}} \quad (74)$$

where \vec{p} consists of the following DMN parameters:

$$\vec{p} = \{z^{k=1, \dots, 2^{N-1}}, \alpha_{i=1, \dots, N}^{k=1, \dots, 2^{i-1}}, \beta_{i=1, \dots, N}^{k=1, \dots, 2^{i-1}}, \gamma_{i=1, \dots, N}^{k=1, \dots, 2^{i-1}}\} \quad (75)$$

For an unseen RVE, the microstructure is first discretized into a mesh and represented as a graph \mathbb{G} . The trained GNN-DMN framework then extracts the corresponding DMN parameters \vec{p} , enabling homogenization without requiring additional parameter fitting, as shown in Fig. 11.

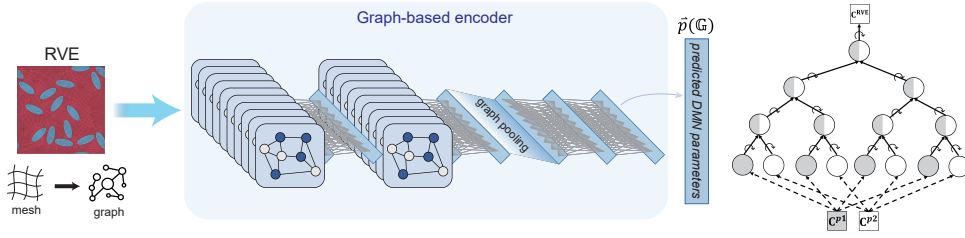


Fig. 11 Schematic illustration of the GNN-DMN framework.

3.2.6 Foundation model-IMN framework

Foundation models (FMs) have achieved remarkable success across various domains, including natural language processing, computer vision, and, more recently, composite materials modeling [38]. In the context of material modeling, a recent study introduced an FM-based approach that leverages a masked autoencoder (MAE)

to learn microstructural representations from a large dataset of 100,000 composite microstructures.

The MAE employs an encoder-decoder architecture for self-supervised learning. During pretraining, a portion of the input microstructure image is masked, and the encoder extracts latent features from the unmasked regions. The decoder then reconstructs the missing parts, compelling the encoder to capture essential structural patterns and dependencies. Through this process, the encoder learns a low-dimensional representation that effectively encodes microstructural information while remaining robust to missing data.

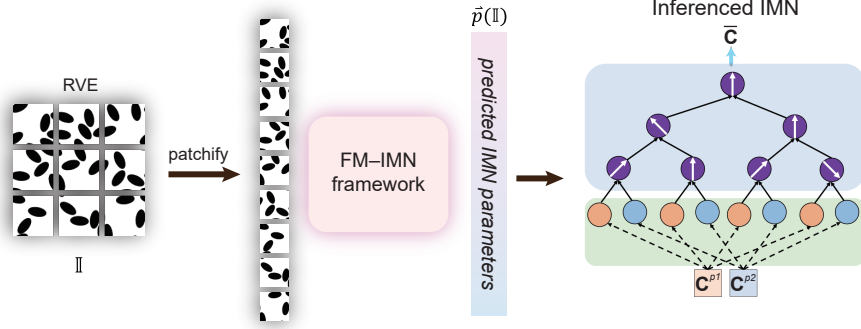


Fig. 12 Schematic illustration of the FM-IMN framework.

Once pre-trained, the MAE encoder is extracted and repurposed for downstream tasks. In the FM-IMN framework, a linear projection layer is appended to the pre-trained encoder, directly mapping microstructural images to IMN parameters, as shown in Fig. 12. This transfer learning approach enables the foundation model to be fine-tuned for homogenization tasks. The homogenization process is formulated as:

$$(\tilde{p}(\mathbb{I}), \mathbf{C}^{p1}, \mathbf{C}^{p2}) \mapsto \bar{\mathbf{C}} \quad (76)$$

where \mathbb{I} is the grayscale image of the microstructure, and $\tilde{p}(\mathbb{I})$ represents the predicted IMN parameters.

For an unseen microstructure, its grayscale image is processed by the fine-tuned FM-IMN framework. Since this framework eliminates the need for explicit parameter fitting for each new microstructure, it enables efficient nonlinear extrapolation across diverse material systems.

4 Applications

DMN have emerged as powerful surrogate models for two-scale analyses, offering substantial computational efficiency while maintaining accuracy. Initially applied to SFRP, their applicability has since expanded across diverse material systems and industrial applications.

A key application of DMNs is in SFRP component analysis [40]. By replacing the conventional RVE with a DMN at each Gaussian integration point, the FE–DMN framework enables efficient multiscale simulations within ABAQUS via an implicit user-material (UMAT) subroutine. In a study on a quadcopter drone with over 9 million DOFs, fiber orientation data from injection molding simulations were incorporated to perform high-fidelity structural analysis. Despite the model’s complexity, the simulation completed in 267 minutes using 252 GB of DRAM, demonstrating the feasibility of DMNs for large-scale industrial applications.

DMNs have also been extended to thermomechanically coupled composite materials [41, 42]. For instance, a non-symmetric notched plate under cyclic loading was analyzed using a two-scale simulation to capture the fully coupled thermomechanical response. Compared to conventional approaches, the DMN-based method achieved a computational speedup of five to six orders of magnitude while preserving accuracy. This capability is particularly relevant for applications involving temperature-dependent material behavior.

Another notable application involves impact and contact simulations of composite structures under dynamic loading. One study integrated fiber orientation and volume fraction data from Moldex3D injection molding simulations into a DMN surrogate model, which was then coupled with LS-DYNA for large-scale impact analysis [43]. This approach enables efficient and accurate simulations of dynamic impact events, offering a computationally viable alternative to conventional multiscale modeling methods. The ability of DMNs to handle large-scale impact scenarios makes them particularly valuable for designing lightweight, crashworthy materials in automotive applications.

Furthermore, DMNs have been employed for inverse identification of material parameters in short fiber-reinforced thermoplastics, a process that remains computationally demanding even with FFT-based methods. By replacing full-field simulations with DMN surrogates, this methodology have significantly reduced computational costs while maintaining high accuracy [44].

In summary, DMNs have proven effective in a wide range of multiscale and multiphysics applications, including structural and thermomechanical analysis, impact modeling, and inverse parameter identification. Their flexibility and computational efficiency make them a promising tool for advanced material modeling and industrial applications, with ongoing research continuously expanding their scope.

5 Conclusion

This study provides a comprehensive overview of the theoretical foundation of DMNs, their adaptations for various material systems, and their capability to model multiphysics phenomena. Additionally, various strategies for extending DMNs to diverse

microstructures are reviewed, along with their applications in FE-DMN frameworks, such as large-scale structural simulations and inverse material parameter identification.

A key advantage of DMNs lies in their hierarchical building-block structure, which enables the explicit derivation of the linear homogenization function. This allows DMNs to be efficiently trained on linear datasets while retaining the capacity for non-linear extrapolation, making them applicable to a broad range of material systems and multiphysics problems. However, a notable limitation is that a trained DMN remains specific to a single microstructure, necessitating retraining for new microstructures. This constraint can be mitigated by incorporating interpolation functions that map microstructural descriptors onto DMN parameters, enhancing their adaptability to complex engineering materials.

With these capabilities, DMNs offer significant potential for industrial applications. Their ability to deliver high-fidelity predictions at reduced computational costs makes them a promising tool for multiscale modeling, materials design, and structural analysis. Future developments in DMN architectures, particularly their integration with commercial simulation platforms, are expected to further extend their practical applications in engineering and industrial settings.

Acknowledgements

This work is supported by the National Science and Technology Council, Taiwan, under Grant 111-2221-E-002-054-MY3 and 112-2221-E-007-028. We are grateful for the computational resources and support from the NTUCE-NCREE Joint Artificial Intelligence Research Center and the National Center of High-performance Computing (NCHC). In addition, we sincerely thank the anonymous reviewers for their constructive comments.

Declarations

The authors declare that they have no known competing financial interests or personal relationships that could have appeared to influence the work reported in this paper.

References

- [1] Hill, R.: A self-consistent mechanics of composite materials. *Journal of the Mechanics and Physics of Solids* **13**(4), 213–222 (1965)
- [2] Feyel, F., Chaboche, J.: Fe2 multiscale approach for modelling the elastoviscoplastic behaviour of long fibre sic/ti composite materials. *Computer Methods in Applied Mechanics and Engineering* **183**(3-4), 309–330 (2000)
- [3] Geers, M., Kouznetsova, V., Brekelmans, W.: Multi-scale computational homogenization: Trends and challenges. *Journal of Computational and Applied Mathematics* **234**(7), 2175–2182 (2010)

- [4] Mohammadpour, A., Geers, M.G., Kouznetsova, V.G.: Multi-scale modeling of the thermo-mechanical behavior of cast iron. *Multiscale Science and Engineering* **4**(3), 119–136 (2022)
- [5] Lee, D., Lee, J.: Comparison and validation of numerical homogenization based on asymptotic method and representative volume element method in thermal composites. *Multiscale Science and Engineering* **3**(2), 165–175 (2021)
- [6] Temizer, I., Wriggers, P.: An adaptive multiscale resolution strategy for the finite deformation analysis of microheterogeneous structures. *Computer Methods in Applied Mechanics and Engineering* **200**(37-40, SI), 2639–2661 (2011) <https://doi.org/10.1016/j.cma.2010.06.013>
- [7] Eisenlohr, P., Diehl, M., Lebensohn, R.A., Roters, F.: A spectral method solution to crystal elasto-viscoplasticity at finite strains. *International Journal of Plasticity* **46**(SI), 37–53 (2013) <https://doi.org/10.1016/j.ijplas.2012.09.012>
- [8] Shanthraj, P., Eisenlohr, P., Diehl, M., Roters, F.: Numerically robust spectral methods for crystal plasticity simulations of heterogeneous materials. *International Journal of Plasticity* **66**(SI), 31–45 (2015) <https://doi.org/10.1016/j.ijplas.2014.02.006>
- [9] Vidyasagar, A., Tutcuoglu, A.D., Kochmann, D.M.: Deformation patterning in finite-strain crystal plasticity by spectral homogenization with application to magnesium. *Computer Methods in Applied Mechanics and Engineering* **335**, 584–609 (2018) <https://doi.org/10.1016/j.cma.2018.03.003>
- [10] Lebensohn, R.A., Rollett, A.D.: Spectral methods for full-field micromechanical modelling of polycrystalline materials. *Computational materials science* **173** (2020) <https://doi.org/10.1016/j.commatsci.2019.109336>
- [11] Zhang, A., Mohr, D.: Using neural networks to represent von mises plasticity with isotropic hardening. *International Journal of Plasticity* **132** (2020) <https://doi.org/10.1016/j.ijplas.2020.102732>
- [12] Mozaffar, M., Bostanabad, R., Chen, W., Ehmann, K., Cao, J., Bessa, M.A.: Deep learning predicts path-dependent plasticity. *Proceedings of the National Academy of Sciences, USA* **116**(52), 26414–26420 (2019) <https://doi.org/10.1073/pnas.1911815116>
- [13] Bishara, D., Xie, Y., Liu, W.K., Li, S.: A state-of-the-art review on machine learning-based multiscale modeling, simulation, homogenization and design of materials. *Archives of Computational Methods in Engineering* **30**(1), 191–222 (2023) <https://doi.org/10.1007/s11831-022-09795-8>
- [14] Frankel, A.L., Jones, R.E., Alleman, C., Templeton, J.A.: Predicting the mechanical response of oligocrystals with deep learning. *Computational Materials Science*

169 (2019) <https://doi.org/10.1016/j.commatsci.2019.109099>

- [15] Chen, Q., Jia, R., Pang, S.: Deep long short-term memory neural network for accelerated elastoplastic analysis of heterogeneous materials: An integrated data-driven surrogate approach. *Composite Structures* **264** (2021) <https://doi.org/10.1016/j.compstruct.2021.113688>
- [16] Kim, D., Lee, J.: A review of physics informed neural networks for multiscale analysis and inverse problems. *Multiscale Science and Engineering*, 1–11 (2024)
- [17] Lee, H., Lee, S., Ryu, S.: Advancements and challenges of micromechanics-based homogenization for the short fiber reinforced composites. *Multiscale Science and Engineering* **5**(3), 133–146 (2023)
- [18] Chang, H.-S., Tsai, J.-L.: Predict elastic properties of fiber composites by an artificial neural network. *Multiscale Science and Engineering* **5**(1), 53–61 (2023)
- [19] Liu, Z., Wu, C.T., Koishi, M.: A deep material network for multiscale topology learning and accelerated nonlinear modeling of heterogeneous materials. *Computer Methods in Applied Mechanics and Engineering* **345**, 1138–1168 (2019) <https://doi.org/10.1016/j.cma.2018.09.020>
- [20] Liu, Z., Wu, C.T.: Exploring the 3d architectures of deep material network in data-driven multiscale mechanics. *Journal of the Mechanics and Physics of Solids* **127**, 20–46 (2019) <https://doi.org/10.1016/j.jmps.2019.03.004>
- [21] Gajek, S., Schneider, M., Böhlke, T.: On the micromechanics of deep material networks. *Journal of the Mechanics and Physics of Solids* **142**, 103984 (2020)
- [22] Glorot, X., Bordes, A., Bengio, Y.: Deep sparse rectifier neural networks. In: *Proceedings of the Fourteenth International Conference on Artificial Intelligence and Statistics*, pp. 315–323 (2011). *JMLR Workshop and Conference Proceedings*
- [23] Bottou, L.: Large-scale machine learning with stochastic gradient descent. In: *Proceedings of COMPSTAT'2010: 19th International Conference on Computational Statistics Paris France, August 22-27, 2010 Keynote, Invited and Contributed Papers*, pp. 177–186 (2010). Springer
- [24] Nguyen, V.D., Noels, L.: Micromechanics-based material networks revisited from the interaction viewpoint; robust and efficient implementation for multi-phase composites. *European Journal of Mechanics - A/Solids* **91**, 104384 (2022) <https://doi.org/10.1016/j.euromechsol.2021.104384>
- [25] Nguyen, V.D., Noels, L.: Interaction-based material network: A general framework for (porous) microstructured materials. *Computer Methods in Applied Mechanics and Engineering* **389**, 114300 (2022) <https://doi.org/10.1016/j.cma.2021.114300>

- [26] Wei, T.-J., Su, T.-H., Chen, C.-S.: Orientation-aware interaction-based deep material network in polycrystalline materials modeling. *Computer Methods in Applied Mechanics and Engineering* **441**, 117977 (2025) <https://doi.org/10.1016/j.cma.2025.117977>
- [27] Li, T.: Micromechanics-informed parametric deep material network for physics behavior prediction of heterogeneous materials with a varying morphology. *Computer Methods in Applied Mechanics and Engineering* **419**, 116687 (2024) <https://doi.org/10.1016/j.cma.2023.116687>
- [28] Shin, D., Alberdi, R., Lebensohn, R.A., Dingreville, R.: A deep material network approach for predicting the thermomechanical response of composites. *Composites Part B: Engineering* **272**, 111177 (2024)
- [29] Shin, D., Creveling, P.J., Roberts, S.A., Dingreville, R.: Deep material network for thermal conductivity problems: Application to woven composites. *Computer Methods in Applied Mechanics and Engineering* **431**, 117279 (2024)
- [30] Liu, Z.: Deep material network with cohesive layers: Multi-stage training and interfacial failure analysis. *Computer Methods in Applied Mechanics and Engineering* **363**, 112913 (2020)
- [31] Liu, Z.: Cell division in deep material networks applied to multiscale strain localization modeling. *Computer Methods in Applied Mechanics and Engineering* **384**, 113914 (2021)
- [32] Sterr, B., Gajek, S., Hrymak, A., Schneider, M., Böhlke, T.: Deep material networks for fiber suspensions with infinite material contrast. *International Journal for Numerical Methods in Engineering* **126**(7), 70014 (2025)
- [33] Wan, W.N., Wei, T.J., Su, T.H., Chen, C.S.: Decoding material networks: exploring performance of deep material network and interaction-based material networks. *Journal of Mechanics* **40**, 796–807 (2024)
- [34] Shin, D., Alberdi, R., Lebensohn, R.A., Dingreville, R.: Deep material network via a quilting strategy: visualization for explainability and recursive training for improved accuracy. *npj Computational Materials* **9**(1), 128 (2023)
- [35] Liu, Z., Wu, C.T., Koishi, M.: Transfer learning of deep material network for seamless structure-property predictions. *Computational Mechanics* **64**(2, SI), 451–465 (2019) <https://doi.org/10.1007/s00466-019-01704-4>
- [36] Huang, T., Liu, Z., Wu, C.T., Chen, W.: Microstructure-guided deep material network for rapid nonlinear material modeling and uncertainty quantification. *Computer Methods in Applied Mechanics and Engineering* **398**, 115197 (2022) <https://doi.org/10.1016/j.cma.2022.115197>

- [37] Jean, J.G., Su, T.H., Huang, S.J., Wu, C.-T., Chen, C.S.: Graph-enhanced deep material network: multiscale materials modeling with microstructural informatics. *Computational Mechanics* **75**, 113–136 (2025)
- [38] Wei, T.-J., Chen, C.-S.: Foundation model for composite microstructures: Reconstruction, stiffness, and nonlinear behavior prediction. *arXiv preprint arXiv:2411.06565* (2024)
- [39] Advani, S.G., Tucker III, C.L.: The use of tensors to describe and predict fiber orientation in short fiber composites. *Journal of rheology* **31**(8), 751–784 (1987)
- [40] Gajek, S., Schneider, M., Böhlke, T.: An fe-dmn method for the multiscale analysis of short fiber reinforced plastic components. *Computer Methods in Applied Mechanics and Engineering* **384**, 113952 (2021) <https://doi.org/10.1016/j.cma.2021.113952>
- [41] Gajek, S., Schneider, M., Böhlke, T.: An fe-dmn method for the multiscale analysis of thermomechanical composites. *Computational Mechanics* **69**(5), 1087–1113 (2022)
- [42] Chatzigeorgiou, G., Charalambakis, N., Chemisky, Y., Meraghni, F.: Periodic homogenization for fully coupled thermomechanical modeling of dissipative generalized standard materials. *International Journal of Plasticity* **81**, 18–39 (2016)
- [43] Wei, H., Wu, C.T., Hu, W., Su, T.-H., Oura, H., Nishi, M., Naito, T., Chung, S., Shen, L.: Ls-dyna machine learning-based multiscale method for nonlinear modeling of short fiber-reinforced composites. *Journal of Engineering Mechanics* **149**(3) (2023) <https://doi.org/10.1061/JENMDT.EMENG-6945>
- [44] Dey, A.P., Welschinger, F., Schneider, M., Gajek, S., Böhlke, T.: Rapid inverse calibration of a multiscale model for the viscoplastic and creep behavior of short fiber-reinforced thermoplastics based on deep material networks. *International Journal of Plasticity* **160**, 103484 (2023)